11

Confocal White Light Reflection Imaging for Characterization of Nanostructures

C. L. Du[1], Y. M. You[2, 3], Z. H. Ni[4], J. Kasim[2] and Z. X. Shen[2]
[1]*College of Science, Nanjing University of Aeronautics and Astronautics, Nanjing*
[2]*Division of Physics and Applied Physics, School of Physical and Mathematical Sciences*
Nanyang Technological University
[3]*Department of Chemistry, Yale University, CT*
[4]*Department of Physics, Southeast University, Nanjing*
[1,4]*PR China*
[2]*Singapore*
[3]*USA*

1. Introduction

The ability to image nanostructures with a high spatial resolution as well as spectral resolution is very important for a host of both fundamental and practical studies (Grigorenko et al., 2005; Dixon et al., 1991; Verveer et al., 2007; Yoshifumi et al., 2006; Singh et al., 2007; Patel & McGhee, 2007; Laurent et al., 2006). Recently, optical imaging and spectroscopic studies of metal nanoarrays, individual metal nanostructures, and graphene (one monolayer thick carbon atoms packed into a two-dimensional honeycomb lattice, which is the basic building block for other sp^2 carbon nanomaterials.) sheet have attracted much attention (Du et al., 2008, 2010; Laurent et al., 2005, 2006; Ni et al., 2007; Wang et al., 2010). As an example, scanning near-field optical microscope (SNOM) has provided high resolution and been widely used in nanostructure study. However, collecting an image by SNOM is very time-consuming and relies heavily on the equipment as well as the skill of the operator. SNOM is also ill-suited for spectroscopic measurements due to the weak signals. Comparatively, far-field techniques are simpler and generate much stronger signals, which have been successfully used to study localized surface plasmons (LSPs) of gold nanoparticle arrays (Laurent et al., 2005, 2006). Moreover, far-field white light scanning is a simple and low cost method, which also offers multiple-wavelength advantage and is suitable to study spectral properties. White light confocal scanning microscopy has also been used to characterize material morphology, refractive index profile of fibers, etc (Ribes et al., 1995; Youk & Kim, 2006), where aperture or fiber were used as confocal pinhole. The best spatial resolution for normal confocal white light scanning optical microscope (not including that from a super continuum light source (Lindfors et al., 2004)) has been improved from 1.500 μm to about 0.800 μm (Youk & Kim, 2006). However, improvement of the spatial resolution is still much desired for the study of small-scale materials.

In this chapter, a new confocal white light reflection imaging technique is proposed by combining a confocal white light scanning microscope with a spectrometer. By decreasing the diameters of the incident light beam and the collection fiber, a spatial resolution of about 0.410 μm was achieved, which doubly enhances the previously reported best spatial resolution (~0.800 μm) of white light scanning and is even higher than those of laser scanning techniques (Rembe & Dräbenstedt, 2006; Gütay and Bauer, 2007). This system can provide both sample images extracted from reflection within a selective range of wavelength and their white light reflection spectra at each point. The simplicity in carrying out experiments makes this technique attractive, easy and fast. Metal nanoarrays, individual metal nanostructures (including single, dimer gold nanospheres and silver nanowires) and graphene sheet were characterized by the proposed system, demonstrating the strong capabilities in resolving nanometre structures, distinguishing different LSP resonant energies between different individual metal nanostructures and determining the graphene number layers, even the refractive index information of graphene.

2. Instrumentation and experiment

The schematic diagram of the experimental setup was shown in Figure 1. Light from a normal white light source (Xenon lamp) was polarized after passing through a polarizer, which serves as the incident light and was focused onto the sample through a holographic beam splitter and an OLYMPUS microscope objective lens (100X, NA=0.95). A tuneable aperture with a minimum diameter of 200 μm was introduced in the incident light path to tune the spatial resolution of the optical system. Different nanostructure samples were placed on a translation stage which provides coarse movement along the x and y axes, while the fine movement is offered by a piezostage with 100 μm travel distance along the x and y directions and 20 μm along the z direction. The piezostage also works as a mapping stage.

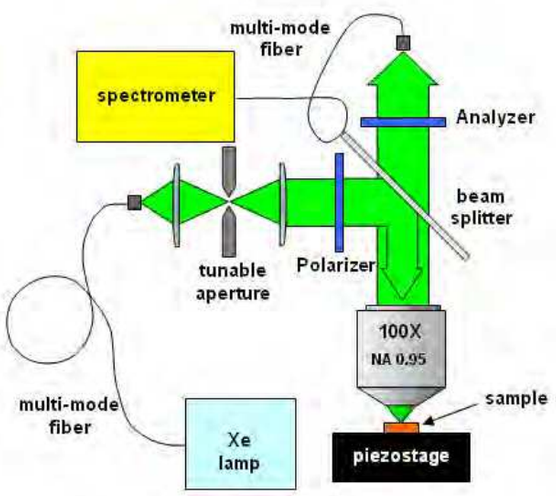

Fig. 1. Schematic diagram of the proposed confocal white light reflection imaging system. (Du et al., 2008).

The reflected light from the sample was collected by the same lens and directed to a spectrometer through a fiber. Fibers with various core diameters of 100, 50 and 25 μm were

adopted in this work. The collection fiber also works as a pinhole, which is confocal with the illuminated spot on the sample. The reflected light was directed to a 150 grooves/mm grating and detected by a TE-cooled charge-coupled device (CCD). Typical integration time for imaging was 100 ms/pixel. The stage movement and data acquisition were controlled using ScanCtrl Spectroscopy Plus software from WITec GmbH, Germany.

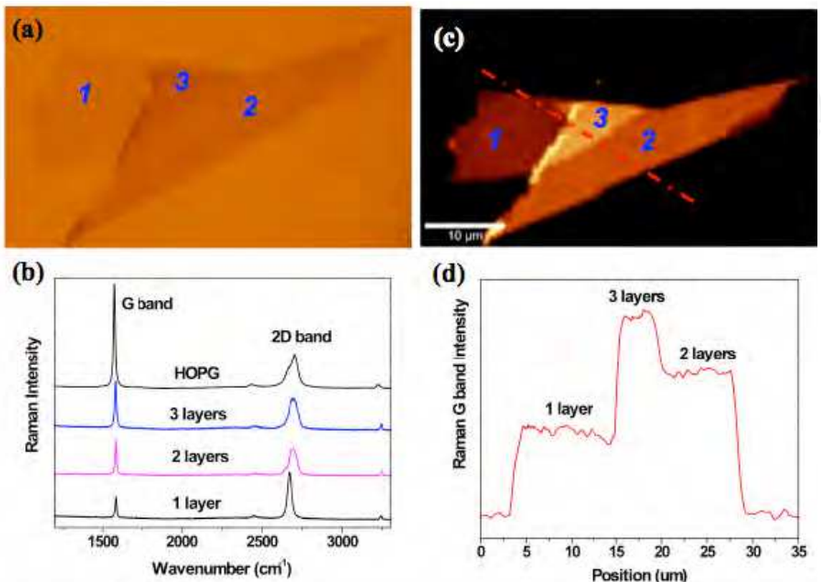

Fig. 2. (a) optical image of 1-, 2-, and 3-layer graphene. (b) Raman spectra of different layer graphene sheets and HOPG. (c) Raman image plotted by the intensity of G-band. (d) Cross section of Raman image, which corresponds to the dashed line in (c).

To determine the spatial resolution of the confocal reflection imaging system, we referred to the scanning knife edge method (Veshapidze et al., 2006) by using a two-layer graphene sheet on SiO_2/Si substrate as the edge (Ni et al., 2007). Thickness of a single layer graphene sheet is ~0.34 nm. The graphene sample was prepared by micromechanical cleavage on a silicon wafer with a 300 nm of SiO_2 capping layer (Novoselov et al., 2004). The optical microscope (Figure 2a) was used to locate the graphene sheet, which thickness was further confirmed by Raman spectroscopy. Figure 2b gives the Raman spectra of the graphene sample while its Raman image plotted by the intensity of G band was shown as Figure 2c. Figure 2d plots the cross section of the Raman image from the dashed line in Figure 2c, showing distinct difference in the Raman G-band intensity from the different thicknesses of graphene sample. Hence, the 2-layer graphene sheet can be identified easily, which provides an ideal edge sample because it has strong enough Raman signal with sharp edge, and most importantly it is thin such that there is no ambiguity in determining the spatial resolution caused by the edge effect.

The scanning confocal white light reflection spectrum by using 25 µm core diameter collection fiber and 200 µm diameter aperture was shown in Figure 3, which was fitted quite well with the following equation:

$$I(x) = \frac{P}{2}\left\{1 + erf\left(\frac{\sqrt{2}(x - x_0)}{w}\right)\right\} \quad (1)$$

where P is the total power for the incident white light beam, x_0 is the centre of the incident light beam and w is the desired $1/e^2$ half width. Thus the full width at half maximum (FWHM) of the incident beam (spot size) can be obtained from $\sqrt{2\ln 2}w$, which was defined as the spatial resolution.

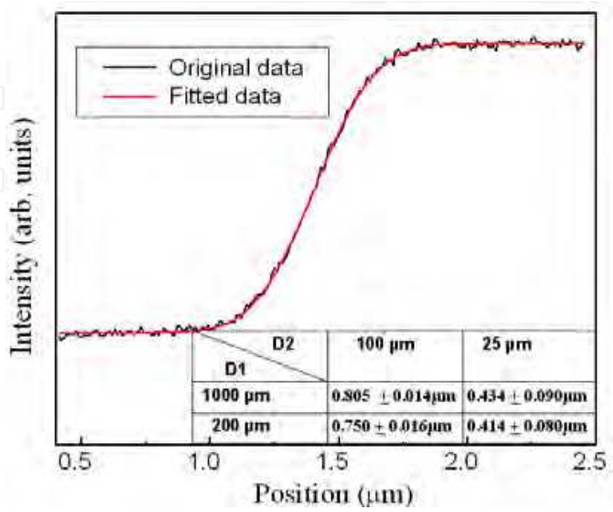

Fig. 3. Typical intensity versus graphene edge position data with the best fitting to Eq. (1) superimposed to determine the white light spot size. The inset gives the spatial resolution fitting results along with the fitting errors by using different aperture and collection fiber sizes.

Through tuning the collection fiber core diameter (D1) and the aperture diameter (D2), different spatial resolutions were obtained from Eq. (1) as shown in the inset table of Figure 3. It reveals the best spatial resolution about 0.410 μm, obtained using the 25 μm core diameter collection fiber and setting the aperture diameter to 200 μm. This doubles the previously reported best spatial resolution (~0.800 μm) for white light scanning (Youk and Kim, 2006) and is even better than those of laser scanning techniques (Rembe & Dräbenstedt, 2006; Gütay and Bauer, 2007). It also indicates that the aperture size, and especially the diameter of collection pinhole (the diameter of the collection fiber in our case), plays a significant role in improving the system resolution. All the white light reflection images shown below were obtained by setting D1 and D2 to 200 μm and 25 μm, respectively, unless stated otherwise. Scanning electron microscope (SEM) images of samples were taken with field emission SEM (JEOL JSM-6700F).

3. Confocal white light reflection (CWLR) imaging for characterization of metal nanostructures

Following, we will discuss our proposed applications in (1) resolving gold nanoarrys, (2) distinguish the resonance energy difference between the isolated single and dimer gold nanoparticles' LSP and revealing the strength of the near-field coupling between individual gold nanospheres and their supporting SiO_2/Si substrate, and (3) correlating the polarization dependent CWLR images of single silver nanowires with the nanowire polarization dependent excitation of surface plasmon (SP).

3.1 CWLR imaging for characterization of gold nanoarrays

Gold nanoparticle arrays were fabricated by nanosphere lithography (Jensen et al., 1999) on cover glass substrates. Polystyrene (PS) microspheres with diameter 1 μm and 0.500 μm were used as masks, which will self-assemble into monolayer spheres on substrates. Gold thin film with thickness of about 0.050 μm was deposited by DC coater sputtering, and then the spheres were lifted off.

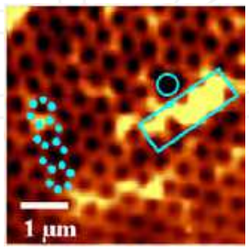

Fig. 4. The CWLR image at the wavelength of 0.480-0.520 μm for gold nanoarrays on cover glass which were fabricated by using 0.500 μm diameter PS as the lithographic mask.

Figure 4 gave a typical 5.0 x 5.0 μm^2 CWLR image for the obtained gold nanoarrays on cover glass fabricated by using 0.500 μm diameter PS as a lithographic mask. The image was extracted from the white light reflection intensity between the wavelength of 0.480-0.520 μm from the samples. Owing to smaller reflection of the cover glass substrate than that of gold particles, hexagonal bright rings in the image of Figure 4 correspond to gold nanoparticles while black areas correspond to the cover glass. The periodicity for the gold particle arrays, which is 0.500 μm, can be clearly resolved, demonstrating the high resolution of our technique. However, the gold particle size and centre-to-centre distance between two nearest gold particles is measured to be about 0.150 μm and 0.100 μm, respectively, by SEM images (not shown), which are out of the range of the system's spatial resolution. This can explain why the image for six gold particles in one hexagonal cell merges to form a hexagonal ring. The dots in Figure 4 work just as a guide for the eye labelling where the particle is. Meanwhile, different defects in the sample as indicated by the rectangular circles in Figure 4 were imaged as well, which reveals that the present imaging method can also be used to test the sample quality, similar to reports elsewhere (Ormonde et al., 2004), but here with much higher spatial resolution.

For comparison, in Figure 5, we have also given the CWLR images for gold nanoarrays on cover glass fabricated by using 1 μm diameter PS as a lithographic mask. Similar to Figure 4, owing to the smaller reflection of the substrate than metal particles, hexagonal bright dots in images Figures 5a to 5f correspond to gold particles while black areas correspond to the cover glass. From the images, we found that the image at 0.480-0.520 μm gives us the best resolution. All the images in this chapter were selected by this way. The gold particle size and centre-to-centre distance between two nearest gold particles is measured to be about 0.300 μnm and 0.200 μm, respectively, by SEM images (not shown). From images in Figures 5a to 5(f), the six gold nanoparticles in one hexagon cell can be resolved clearly as labelled by pink dots in Figure 5a for guiding. The size of these six nanoparticles in CWLR images is spatial resolution determined, which is ~0.410 μm. From these images, it is very easy to obtain the white light reflection spectra for the substrate and gold particles, respectively, as shown in Figure 5g. The contrast spectra are defined as

$$Contrast = (I_{sample} - I_{substrate}) / I_{substrate} \quad (2)$$

where I_{sample} and $I_{substrate}$ refer to the white light reflection intensity of the sample and the substrate, respectively. The result was shown as Figure 5h, which confirms that gold particles always have larger reflection than that of the substrate, as well as the role of SP in reflection, which is discussed in detail in the next section.

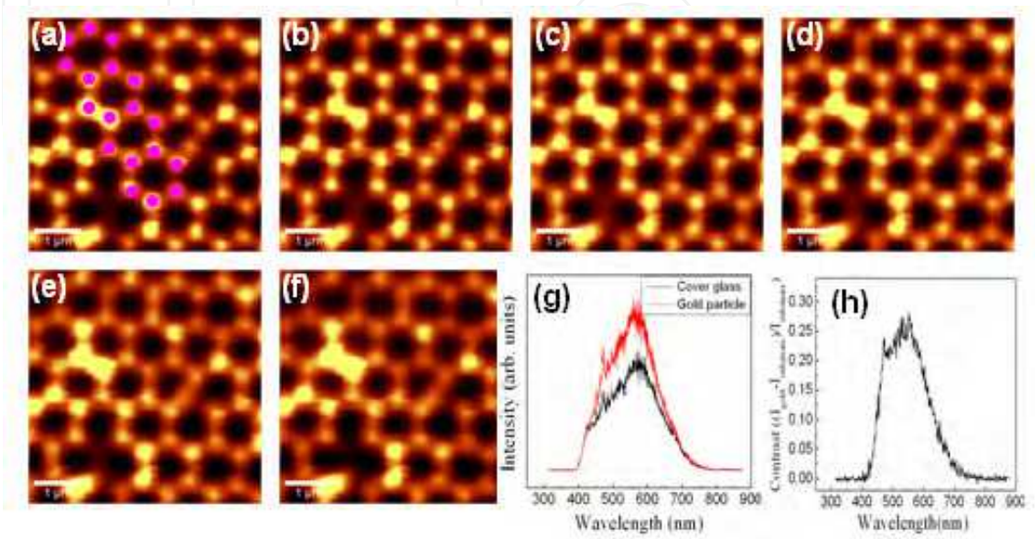

Fig. 5. The CWLR images (a-f) at different wavelength ranges for gold nanoarrays on cover glass fabricated by using 1 μm diameter PS as the lithographic mask while (g) and (h) are the reflected white light spectra and reflection contrast between the gold particle and substrate, respectively. Wavelength ranges for images (a) to (f) correspond to 0.440-0.480 μm, 0.480-0.520 μm, 0.520-0.560 μm, 0.560-0.600 μm, 0.600-0.640 μm and 0.640-0.680 μm, respectively.

3.2 CWLR imaging for characterization of individual gold nanospheres

Commercial gold nanospheres with a diameter of 50 ± 5 nm (Corpuscular Inc) deposited on 200 nm silicon dioxide (SiO_2) films were chosen for CWLR imaging as well. Their confocal white light reflection images were constructed by extracting the light intensity from the corresponding reflection spectra for a selected wavelength range, too. The image at the wavelength of 510-550 nm was shown in Figure 6b as one example. As can be seen from the SEM image shown in Figure 6a, it consists of three isolated single spheres and one dimer where the two spheres are almost in contact with each other. The four dark spots in Figure 6b represent the images of the gold nanospheres, which correspond well to the SEM image. The size of the dark spots is about 410 nm, determined by the spatial resolution of the imaging system. Considering the resolution limitation, it is reasonable that the white light reflection images can not distinguish between single sphere and dimer spheres. For comparison, Figure 6d presented the CWLR imaging results for the spheres by setting D2 to 100 μm while keeping other experimental conditions the same. It can be seen that the images from the spheres severely overlap, confirming the higher spatial resolution by using a 25 μm core diameter collection fiber again.

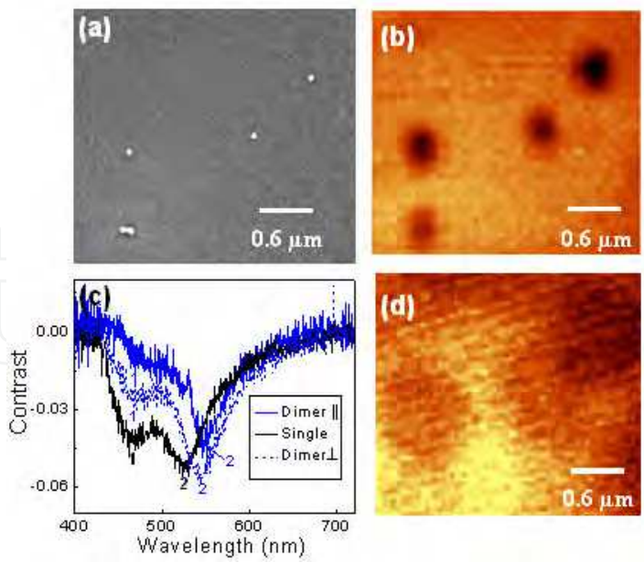

Fig. 6. SEM image (a) and CWLR images at wavelength 510-550 nm of gold nanospheres on 200 nm SiO_2 films with collection fiber core diameter 25 μm (b) and 100 μm (d). (c) The contrast spectra for single (black lines) and dimer spheres for incident light parallel (solid lines) and perpendicular (dotted lines) to the dimer axis. (Du et al., 2008).

Figure 6c plotted the contrast spectra for the single and dimer gold nanospheres after locating their positions. Two contrast dips (labelled 1 and 2, respectively) were observed from Figure 6. It is noticed that the position of dip 2 of isolated single spheres (at about 525 nm) coincides with that of the LSP of gold spheres with diameter 50 nm (Dijk et al., 2005). However, the same dip shows red shifts to 548 nm and 542 nm for the incident polarization parallel and perpendicular to the dimer axis, respectively. This results from the coupling effect between the two nanospheres of the dimer (Moores & Goettmann, 2006). The larger red shift for the parallel polarization than that of the perpendicular case is understandable considering the stronger coupling of the dimer for parallel polarization. Figure 6c also reveals a weak dip 1 for the single and dimer located at about 470 nm, which originates from the multi-polar SP excitation of the gold nanospheres. Firstly, SP excitation at about 470 nm has been observed for gold nanospheres with diameters close to 40 nm, although it was ascribed to false spectral lines that arose from using a 488 nm argon laser (Benrezzak et al., 2001). Secondly, similar multi-polar SP excitation has been reported for other isolated metal nanoparticles (Dijk et al., 2005). Moreover, the excitation of LSPs leads to the enhancement of the absorption of the nanospheres, which consequently has the effect of reducing the reflection intensity (Kawata, 2001), making the nanospheres dark in the corresponding images in Figure 6b. The different dip 2 position for the single and dimer spheres also reflects their different dipolar LSP resonant energies, further implying that the CWLR imaging method is capable of resolving the LSP energies for individual noble metal nanoparticles.

Then, to determine the decay length of the electromagnetic (EM) coupling between individual gold nanopspheres and its supporting substrate, different thicknesses (d) SiO_2 film on Si were obtained by annealing single-crystalline Si (d < 20 nm) in air or by RF sputtering SiO_2 (d > 20 nm) to serve as the substrate.

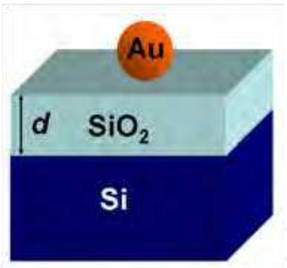

Fig. 7. Schematic diagram of the prepared gold nanospheres on SiO_2/Si substrate samples.

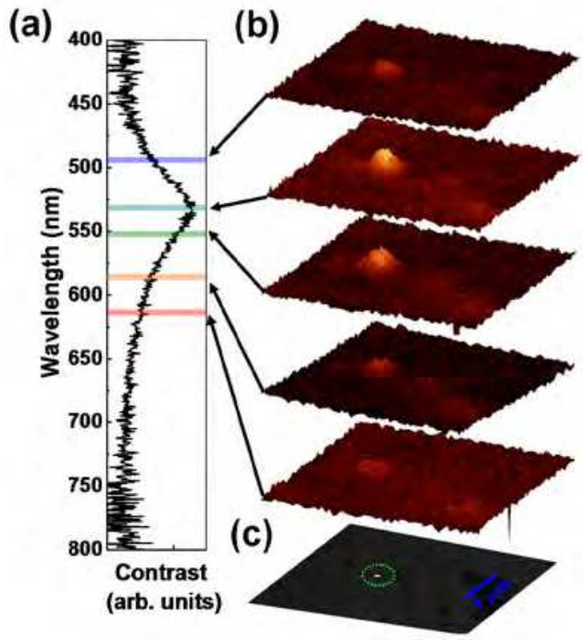

Fig. 8. Comparison between the CWLR contrast images (b) of an individual Au nanosphere on a SiO_2/Si substrate (with SiO_2 film 60 nm) at different selected wavelength regions labelled by the rectangular bars on the corresponding contrast spectra (a) along with the corresponding SEM image of the nanoshpere (c). (Du et al., 2010).

Figure 7 illustrated the schematic diagram of the prepared gold nanospheres on SiO_2/Si substrate samples and a typical SEM image was shown as Figure 8c. The distance between different individual nanospheres chosen for study herein was selected purposely to be larger than 1μm. Thus the EM coupling between them can be neglected. For convenience, herein the contrast is defined by the following Eq. (3), and hence their contrast images and the CWLR contrast spectra can be obtained.

$$Contrast = (I_{sub} - I_{AuNSP}) / I_{sub} \tag{3}$$

Where I_{AuNSP} and I_{sub} refer to the CWLR intensity from the positions of the Au NP and the substrate, respectively. Adopting Eq. (3), the CWLR contrast spectra for individual gold nanoparticles were obtained. A typical CWLR contrast spectra of an individual Au nanosphere on SiO_2/Si substrates was presented as Figure 8a along with its different CWLR

images at different wavelength regions. The different wavelength regions constructing these contrast images were labelled by the rectangular bars on the left contrast spectra of Figure. 8a. Figure 8a presents an obvious peak at ~530 nm, which originates from the excitation of dipolar LSPs with the peak wavelengths corresponding to the dipolar LSP wavelengths (Du et al., 2008; Okamoto & Yamaguchi, 2003; Abe & Kajikawa, 2006; Pinchuk et al., 2004; Knight et al., 2009). The excitation of LSP enhances the light absorption by the nanosphere and reduces its reflection intensity (Kawata, 2001), then further leads to its higher contrast intensity relative to the substrate in the CWLR contrast images (Figure. 8b). As can be seen, with the selected wavelength region closer to the contrast peak position, the larger image contrast between the Au nanosphere and the substrate is obtained while the maximum contrast is reached at the LSP wavelength. Meanwhile, from the unequivocal one-to-one correspondence between the nanosphere in the contrast images (Figure. 8b) and its SEM image (Figure. 8c), we can locate the individual nanosphere we concern.

To explore the near-field coupling between individual gold nanospheres and their supporting substrate further, we have measured the contrast spectra between individual Au nanospheres on SiO_2/Si substrates with different thicknesses of SiO_2 on Si substrate. Several typical spectra were presented in Figure 9, in which the dipolar LSP peaks were guided by the dashed line. The second peak at shorter wavelength for cases of bare Si substrate and d = 6 nm corresponds to the multi-polar LSP excitation (Du et al., 2008). In what follows, we will mainly discuss the dipolar LSP (labelled as LSP for short in the following) wavelength (λ) behaviour as a function of the spacer SiO_2 film thickness d.

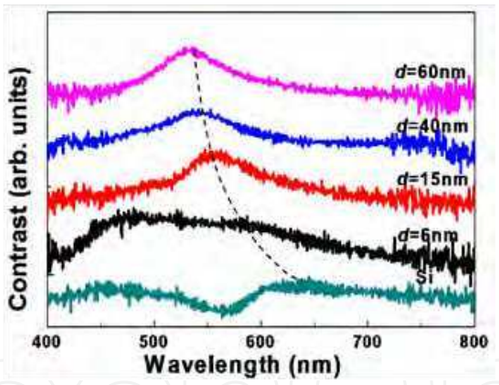

Fig. 9. Comparative CWLR contrast spectra between individual Au nanospheres on SiO_2/Si substrates (with SiO_2 film d nm) and on Si substrate. (Du et al., 2010).

Figure 9 reveals that the LSP wavelengths of all the samples show an obvious red-shift compared to the LSP resonant wavelength for an isolated Au nanosphere with diameter about 50 nm in air, which is at about 520 nm (Noguez, 2007). This originates from the different dielectric function of the substrate from that of air and agrees well with the literature reports (Okamoto & Yamaguchi, 2003; Abe & Kajikawa, 2006; Pinchuk et al., 2004). Moreover, the dashed line in Figure 9 demonstrates that the LSP wavelength blue-shifts with d increasing. To see this more clearly, we have plotted the function of the resonant wavelength λ of these LSP modes versus d in Figure 10. The experimental data of λ vs. d is noted to can be fitted with a single exponential decay function (the solid line) quite well. All these reflect the near-field EM interaction between the nanosphere and its supporting

substrate, which dominates the corresponding LSP wavelength shift (Jain et al., 2007; Biring et al., 2008). Accordingly, the near-field EM coupling strength between them determines the magnitude of the dipolar LSP wavelength shift ($\Delta\lambda = \lambda - \lambda_0$) compared to the LSP wavelength (λ_0) of the isolated nanosphere case.

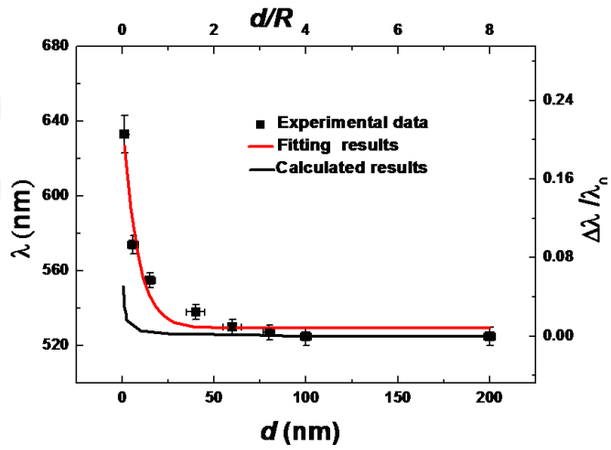

Fig. 10. The function of the LSP wavelength λ versus the spacer thickness *d* (left y-axis and bottom *x*-axis) and the function of the normalized LSP wavelength shift of $\Delta\lambda / \lambda_0$ versus the normalized spacer thickness *d/R* (right y-axis and top *x*-axis): the squared dots, dotted line and solid line correspond to the experimental data, calculated results and the single exponential decay fitting results, respectively). (Du et al., 2010).

By bringing a metal nanoparticle into the vicinity of a flat substrate, nonhomogeneous optical response due to the polarizability of the substrate material is expected. Generally, with an external EM field, a charge polarization on the NP can be induced, which further causes a charge distribution on the substrate. Under the quasi-static approximation, this charge distribution can be seen as the image charge distribution (Okamoto & Yamaguchi, 2006; Noguez, 2007) of the nanoparticle and it can in turn affect the local EM field around the nanoparticle, and further their optical responses. Adopting the method proposed elsewhere (Okamoto & Yamaguchi, 2006; Wind et al., 1987), the extinction spectra of the concerned nanospheres were calculated by including both the dipole and higher multiple image-charge effects along with the Fresnel reflection effect at the nanosphere-substrate interface. The corresponding obtained function of the LSP wavelength (λ) versus the spacer thickness (*d*) was plotted as the dashed line in Figure 10 as well for comparison. The calculation qualitatively verifies the decrease behaviour of the experimental data of λ versus *d* though it predicts a faster decay rate than the experimental results.

To quantify the near-field EM coupling strength between the individual nanosphere and its supporting substrate, the normalized LSP wavelength shift ($\Delta\lambda / \lambda_0$) was calculated as well by the quasi-static theory and for the experimental data. Experimentally, λ_0 is obtained by assuming that it equals to the LSP wavelength of the nanosphere on very thick SiO_2 film (take it as 200 nm). Through a simple linear transformation, both the experimental and theoretical data of λ versus *d* can be transferred into $\Delta\lambda / \lambda_0$ versus *d/R*. The obtained results were scaled according to the right *y*-axis (corresponds to the upper *x*-axis) in Figure 10. It can be seen that $\Delta\lambda / \lambda_0$ decreases with *d/R* and reaches zero for large enough *d/R*. This

demonstrates that the strength of the near-field EM coupling owing to the substrate effect decreases with d/R and then vanishes with further increasing d/R. For thicker spacer ($d > 3R$), the influence of the image-charges owing to the substrate presence is ignorable and the LSP wavelength approaches to the limit of the individual nanosphere in the background. Meanwhile, the faster decay rate of the shift predicted by the quasi-static theory is resulted from the limitation of the theoretical model, which ignores the retardation effect while such effect is more pronounced for larger nanoparticles (Okamoto & Yamaguchi, 2003; Noguez, 2007). The solid line in the right y-axis of Figure 10 presents the single exponential decay fitting by Eq. (4)

$$y = a * \exp(-\frac{x}{t}) + y_0 \tag{4}$$

to the experimental data with a, t and y_0 as the fitting parameters. It reveals a decay length t about 0.30 in units of d/R and the fitting goodness equals to 0.97. The fitting results are interestingly noted to qualitatively agree with the 'plasmon ruler' scaling theory for the near-field EM coupling between two component noble metal nanoparticles of a dimer (Jain et al., 2007). It points out that the decay length is about 0.20 in units of the 'Gap/Diameter' regardless of the nature of the component metal nanoparticles of the dimer (Jain et al., 2007). The similarity of the decay length in magnitude is owing to that the image-charges induced in the substrate can be just replaced by the actual charges induced in the other particle for the dimeric nanoparticle's case. The deviation between their decay lengths is understandable considering the different polarizabilities between the dimer and our case. Thus, the near-field coupling strength between the individual Au nanosphere and the Si substrate is revealed to exponentially decrease with the spacer (SiO_2 film) thickness and the decay length is about 0.3 in units of d/R.

3.3 CWLR imaging for characterization of individual silver nanowires

Silver nanowire samples with a diameter about 100 nm were fabricated by a simple hydrothermal method (Wang et al., 2005) and deposited onto silicon for CWLR imaging. Two typical CWLR images of the silver nanowire were presented as Figures 11a and 11b, which clearly exhibits polarization dependent. By rotating 90 degree of the incident polarization, their contrast reverses from the comparison between Figures 11a and 11b. Even for the same bent nanowire, the different parts exhibits different contrast compared to the substrate. Owing to the larger reflectivity of silver than that of the substrate silicon, it is expected that the nanowires are brighter than the substrate under CWLR imaging system. However, this contradicts with the results of Figure 11, revealing that other factors besides material reflectivity contribute to the observed CWLR images.

It is known that the excitation of SPs of sliver nanowires is anisotropic (Schider et al., 2003), which is sensitive to the polarization direction of the incident light. This can account for the polarization dependence of the reflection images of Figure. 11, which also contribute to the different contrast for different parts of the same bent nanowire as well since for different parts of the same nanowire, the only difference lies in their different orientation relative to the incident light polarization direction. As the images shown in Figures 11a and 11b were extracted from the reflections in the range of 600 – 640 nm, it is overlapped with one of the SP mode (500 – 700 nm) (Kim et al., 2003; Mohanty et al., 2007) of the Ag nanowire, which

experiences preferred excitation when the polarization of the incident light is parallel to the nanowire. Thus, this SP mode along the different material reflectivity contributes to the obtained polarization dependent CWLR images. It also demonstrates that the developed CWLR imaging system is able to correlate the polarization dependent CWLR images of single silver nanowires with the nanowire polarization dependent excitation of SP.

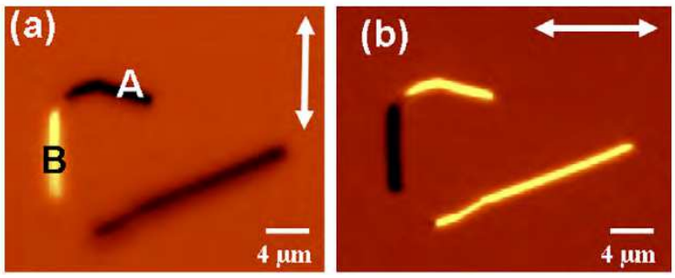

Fig. 11. The CWLR images at the wavelength of 600 – 640 nm for silver nanowires on silicon substrate. The double-direction arrows in the figure indicate the polarization direction of the incident light. (Du et al., 2008).

4. CWLR imaging for characterization of graphene

We also note that the proposed CWLR system is not limited to characterize metal nanostructures. It can also be extended to other samples, such as graphene sheet. In this part, we will show how the system was used to determine the number of graphene layers and to extract the corresponding refractive index.

The graphene's visibility strongly varies from one laboratory to another and it relies on experience of the observer though one can observe different colours/contrasts for graphene sheets of different thickness using the optical image with "naked eyes". Taking advantage of contrast spectra and image, this can be made quantitative and accurate. By combing Raman spectroscopy and optical images, graphene sheets with different layer numbers were first obtained as shown in Figure 12. Then, their contrast spectra were measured and plotted in Figure 12. For consistence with reference (Ni et al., 2007), the contrast spectra C(λ) were obtained by using C(λ)= (R0(λ)- R(λ))/ R0(λ), where R0(λ) is the reflection spectrum from the SiO_2/Si substrate while R(λ) is the reflection spectrum from graphene sheet. As revealed in Figure 12, the contrast spectrum of single layer graphene has a peak at about 550 nm, which makes the single layer graphene visible and is in green-orange range. Meanwhile, the peak position is almost unchanged with increasing number of layers up to ten. The contrast value for single layer graphene is about 0.09+0.005 and it increases with the number of layers, for example, 0.175+0.005, 0.255+0.010, and 0.330+0.015 for two, three, and four layers, respectively. For graphene of around ten layers, the contrast saturates and the contrast peak shifts towards red (samples a and b). For samples with larger number of layers (c to f), negative contrast occurs. This can easily be understood that these samples are so thick that the reflections from their surface become more intense than that from the substrate, resulting in negative value contrast.

Hence, different layer graphene gets different contrast value, which provides a standard for determining the number of layers for graphene. This can also be understood in terms of the

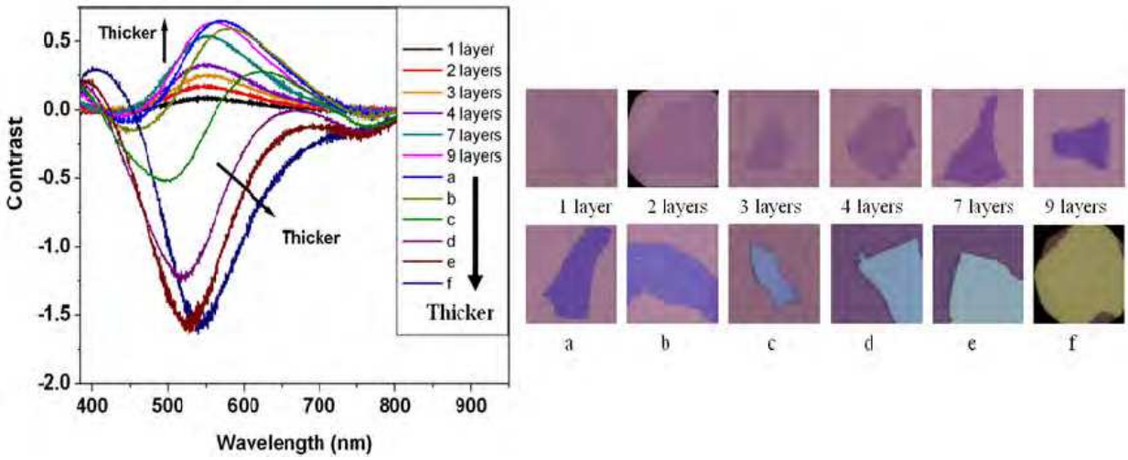

Fig. 12. The contrast spectra of graphene sheets with different thicknesses, together with the optical image of all the samples. Besides the samples with 1, 2, 3, 4, 7 and 9 layers, samples a, b, c, d, e and f are more than ten layers and the thickness increases from a to f. The arrows in the graph show the trend of curves in terms of the thicknesses of graphene sheets. (Ni et al., 2007).

Fresnel reflection theory. Consider the incident light from air (n_0 = 1) onto a graphene, SiO_2, and Si tri-layer system. The reflected light intensity from the tri-layer system can then be described by (Blake et al., 2007; Anders, 1967):

$$R(\lambda) = r(\lambda)r^*(\lambda) \tag{5}$$

$$r(\lambda) = \frac{r_a}{r_b} \tag{6}$$

$$r_a = (r_1 e^{i(\beta_1+\beta_2)} + r_2 e^{-i(\beta_1-\beta_2)} + r_3 e^{-i(\beta_1+\beta_2)} + r_1 r_2 r_3 e^{i(\beta_1-\beta_2)}) \tag{7}$$

$$r_b = (e^{i(\beta_1+\beta_2)} + r_1 r_2 e^{-i(\beta_1-\beta_2)} + r_1 r_3 e^{-i(\beta_1+\beta_2)} + r_2 r_3 e^{i(\beta_1-\beta_2)}) \tag{8}$$

where $r_1 = \frac{n_0 - n_1}{n_0 + n_1}, r_2 = \frac{n_1 - n_2}{n_1 + n_2}, r_3 = \frac{n_2 - n_3}{n_2 + n_3}$ are the reflection coefficients for different interfaces and $\beta_1 = 2\pi n_1 \frac{d_1}{\lambda}, \beta_2 = 2\pi n_2 \frac{d_2}{\lambda}$ are the phase difference when the light passes through the media which is determined by the path difference of two neighbouring interfering light beams. The thickness of the graphene sheet can be estimated as $d1 = N\Delta d$, where N represents the number of layers and Δd is the thickness of single layer graphene (Δd = 0.335 nm) (Kelly, 1981, Dresselhaus, 1996). The refractive index of graphene is used as a fitting parameter. The thickness of SiO_2, d_2, is 285 nm, with a maximum 5% error. The refractive index of SiO_2, n_2, is wavelength dependent (Palik, 1991). The Si substrate is considered as semi-infinite and the refractive index of Si, n_3, is also wavelength dependent (Palik, 1991). The reflection from SiO_2 background, R0(λ), was calculated by setting $n_1 = n_0 = 1$, and $d_1 = 0$.

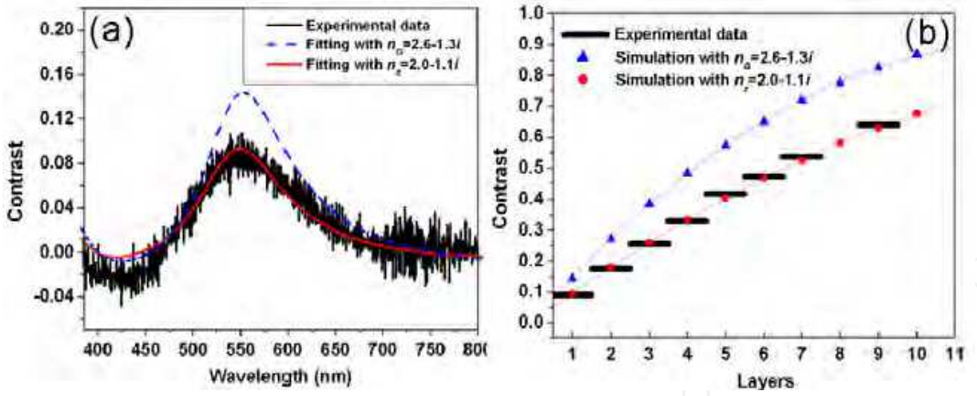

Fig. 13. (a) The contrast spectrum of experimental data (black line), the simulation result using n_z =2.0-1.1i (red line), and the simulation result using n_G = 2.6-1.3i (dash line). (b) The contrast simulated by using both n_G (blue triangles) and n_z (red circles), the fitting curve for the simulations (blue and red lines), and our experiment data (black thick lines), respectively, for one to ten layers of graphene. (Ni et al., 2007).

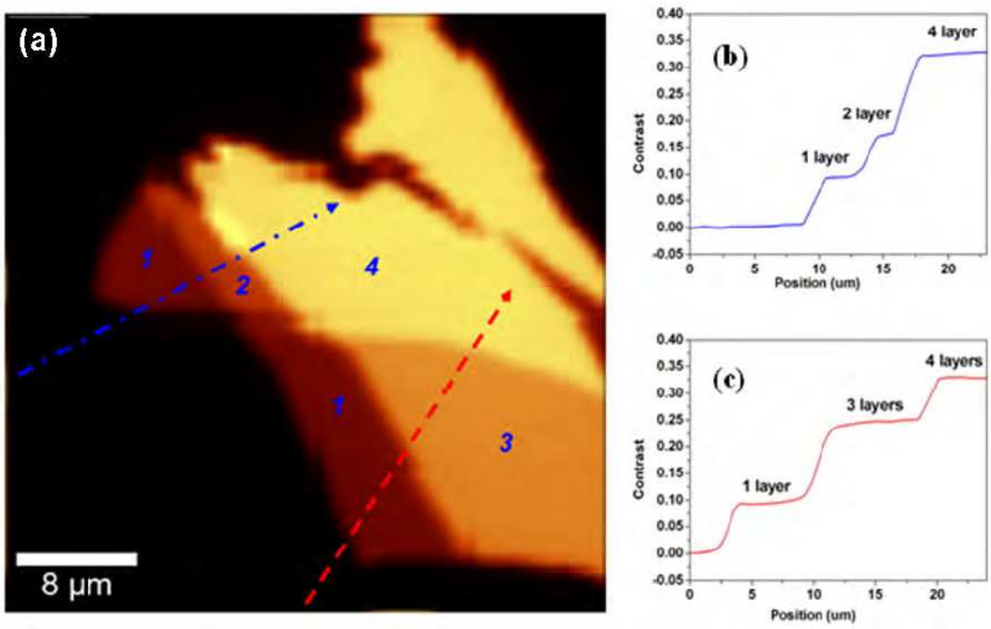

Fig. 14. (a) The contrast image of the sample. (b) and (c) The cross section of contrast image, which corresponds to the dash lines. (Ni et al., 2007).

The optimized simulation result is shown in Figure 13a reveals a refractive index of single layer graphene n_z = 2.0-1.1i, whereas the simulation result using the bulk graphite value of n_G (2.6-1.3i) shows large deviation from our experimental data. Using the optimized refractive index n_z, we have calculated the contrast of one to ten layers' graphene also as shown in Figure 13b, which agree well with the experimental data with the discrepancy being only 2%. By using this technique, the thickness of unknown graphene sheet can be determined directly by comparing the contrast value with the standard values shown in Figure 13b. Alternatively, it can be obtained using the following equation:

$$C = 0.0046+0.0925N-0.00255N^2 \quad (9)$$

where N ($\leq$10) is the number of layers of graphene.

In order to demonstrate the effectiveness of the contrast spectra in graphene thickness determination, we carried out the CWLR imaging, too. As shown in Figure 14a, distinct contrast for different thicknesses of graphene can be observed from the image. It is worth noting that the contrast image measurement can be done in a few minutes. Figure 14b and 14c show contrast along the two dash lines on the image. The contrast value for each thickness agrees well with those shown in Figure 13. Using Eq. (9), the N values along the two dash lines are calculated, where the N along the blue line is: 0.99, 1.93, and 3.83; and along the red line is: 0.98, 2.89 and 3.94. Again our results show excellent agreement.

Accordingly, by the proposed CWLR system, both the layer number of graphene and the refractive index of single layer graphene can be achieved. It does not need a single layer graphene as reference as that in Raman. It is also noted that the proposed system can be used to get information about the optical conductivity of some bilayer grapene sheet (Wang et al., 2010), which is not shown here.

5. Conclusion

In this chapter, we have proposed a far-field CWLR imaging system by combing a small aperture and a small collection fibre core diameter, which is fast, non-destructive and user friendly. It is demonstrated to provide a high spatial resolution about 410 nm, which is capable of resolve two nearest gold nanoparticles with the size and centre-to-centre distance in-between about 300 nm and 200 nm, respectively. Individual single, dimer gold nanospheres, silver nanowires, and graphene sheet were characterized by the imaging system as well. Apart from the dipolar LSP, excitation of multi-polar LSP of individual gold nanospheres was revealed. Compared to the resonance energy of single gold nanosphere, the resonance energy of the dimer is red-shifted due to the EM coupling between the two component nanospheres of the dimer. The near-field EM coupling effect between individual Au nanospheres and the supporting SiO_2/Si substrate was also studied by the CWLR imaging method, which reveals a decay length of 0.30 in units of d/R for the coupling strength, qualitatively agreeing well with the 'plasmon ruler' scaling theory. The anisotropic excitation of LSP of single silver nanowire was revealed to get contribution to the polarization dependent images besides their essential reflectivity difference from that of the substrate. It is also demonstrated that the CWLR spectra method provides a standard to identify the thickness of graphene sheet on Si substrate with ~300 nm SiO_2 capping layer, from which the refractive index (n_z = 2.0-1.1i) of graphene below ten layers can also be easily determined. As the CWLR imaging can be preformed at different wavelength, we also expect its other interesting applications such as biomaterial mapping and plasmonic studies in the future.

6. Acknowledgment

This work was financially supported by the Natural Science Foundation of China (No. 11004103), China Postdoctoral Science Foundation funded project (No. 20100471332), Jiangsu Planned Projects for Postdoctoral Research Funds (No. 0902016C), NUAA Research Funding (No. NS2010186), and NUAA Scientific Research Foundation.

7. References

Abe S.; Kajikawa K. (2006). Linear and Nonlinear Optical Properties of Gold Nanospheres Immobilized on a Metallic Surface. *Phys. Rev. B.*, Vol.74, No.3, pp. 035416, ISSN 1098-0121

Anders H. (1967). *Thin Films in Optics*, Focal Press, London

Benrezzak S.; Adam P. M.; Bijeon J. L.; Royer P. (2001). Observation of Nanometric Metallic Particles with an Apertureless Scanning Near-field Optical Microscope. *Surf. Sci.*, Vol. 491, No.1-2, pp. 195-207, ISSN 0039-6028

Biring S.; Wang H. H; Wang J. K; Wang Y. L. (2008). Light Scattering from 2D Arrays of Monodispersed Ag-nanoparticles Separated by Tunable Nano-gaps: Spectral Evolution and Analytical Analysis of Plasmonic coupling. *Opt. Express*, Vol.16, No.20, pp.15312-15324, ISSN 1094-4087

Blake P.; Hill E. W.; Neto A. H. C.; Novoselov K. S.; Jiang D.; Yang R.; Booth T. J.; Geim A. K. (2007). Making graphene visible. *Appl. Phys. Lett.*, Vol.91, No.6, pp. 063124, ISSN 0003-6951

Dixon A. E.; Damaskinos S.; Atkinson M. R. (1991). A Scanning Confocal Microscope for Transimission and Reflection Imaing. *Nature (London)*, Vol.351, No.6327, pp. 551-553, ISSN 0028-0836

Dijk M. A.; Lippitz M.; Orrit M. (2005). Far-Field Optical Microscopy of Single Metal Nanoparticles. *Acc. Chem. Res.*, 2005, Vol. 38, No. 7, pp. 594–601, ISSN 0001-4842

Dresselhaus M. S.; Dresselhaus G.; Eklund P. C. (1996). *Science of Fullerenes and Carbon Nanotubes*, Academic Press, ISBN 012-221820-5, San Diego, CA

Du C. L.; You Y. M.; Kasim J.; Ni Z. N.; Yu T.; Wong C. P.; Fan H. M.; Shen Z. X. (2008). Confocal White Light Reflection Imaging for Characterization of Metal Nanostructures, *Opt. Commun.* Vol. 281, No.21, pp. 5360-5363, ISSN 0030-4018

Du C. L.; You Y. M.; Kasim J.; Hu H. L.; Zhang X. J.; Shen Z. X. (2010). Near-field Coupling Effect between Individual Au Nanospheres and Their Supporting SiO_2/Si Substrate, *Plasmonics*, Vol. 5, No.2, pp. 105-109, ISSN 1557-1955

Grigorenko A. N.; Geim A. K.; Gleeson H. F.; Zhang Y.; Firsov A. A.; Khrushchev I. Y.;. Petrovic J. (2005). Nanofabricated Media with Negative Permeability at Visible Frequencies. *Nature,* Vol. 438, No. 7066, pp. 335-338, ISSN 0028-0836

Gütay L.; Bauer G. H. (2007). Spectrally Resolved Photoluminescence Studies on Cu(In,Ga)Se2 Solar Cells with Lateral Submicron Resolution. *Thin Solid Films,* Vol. 515, No. 15, pp. 6212-6216, ISSN 0040-6090

Jain P. K.; Huang W. Y.; El-Sayed M. A. (2007). On the Universal Scaling Behavior of the Distance Decay of Plasmon Coupling in Metal Nanoparticle Pairs: a Plasmon Ruler Equation. *Nano lett.* Vol.7, No.7, pp. 2080-2088, ISSN 1530-6984

Jensen T. R.; Duval M. L.; Kelly K. L.; Lazarides A. A.; Schatz G. C.; Duyne RP. Van. (1999). Nanosphere Lithography: Effect of the External Dielectric Medium on the Surface Plasmon Resonance Spectrum of a Periodic Array of Silver Nanoparticles. *J. Phys. Chem. B.*, Vol.103, No., pp. 9846-9853, ISSN 1089-5647

Kawata S. (2001). *Near-field Optics and Surface Plasmon Polaritons*, Springer, ISBN 3540415025, Verlag Berlin Heidelberg

Kelly, B. T. (1981). *Physics of Graphite*, Applied Science, ISBN 0853349606, London

Knight M. W.; Wu Y. P.; Lassiter J. B.; Nordlander P.; Halas N.J. (2009). Substrates Matter: Influence of an Adjacent Dielectric on an Individual Plasmonic Nanoparticle. *Nano Lett.* Vol.9, No. 5, pp.2188–2192, ISSN 1530-6984

Laurent G.; Félidj N.; Truong S. L.; Aubard J.; Lévi G.; Krenn J. R.; Hohenau A.; Leitner A.; Aussenegg F. R. (2005). Imaging Surface Plasmon of Gold Nanoparticle Arrays by Far-field Raman Scattering. *Nano Lett.*, Vol.5, No.2, pp. 253-258, ISSN 1530-6984

Laurent G.; Félidj N.; Grand J.; Aubard J.; Lévi G.; Hohenau A.; Aussenegg F. R.; Krenn J. R. (2006). Raman Scattering Images and Spectra of Gold Ring Arrays. *Phy. Rev. B.*, Vol.73, No.24, pp. 245417, ISSN 1098-0121

Lindfors K.; Kalkbrenner T.; Stoller P.; Sandoghdar V. (2004). Detection and Spectroscopy of Gold Nanoparticles Using Supercontinuum White Light Confocal Microscopy. *Phys. Rev. Lett.*, Vol.93, No.3, pp. 037401, ISSN 0031-9007

Mohanty P.; Yoon I.; Kang T.; Seo K. YT.; Varadwaj K.S.; Choi W. J.; Park Q. H.; Ahn J. P.; Suh Y. D.; Ihee H.; Kim B. (2007). Simple Vapor-phase Synthesis of Single-crystalline Ag Nanowires and Single-nanowire Surface-enhanced Raman Scattering. *J. Am. Chem. Soc.*, Vol.129, No.31, pp. 9576, ISSN 0002-7863

Moores A.; Goettmann F. (2006). The Plasmon Band in Noble Metal Nanoparticles: an Introduction to Theory and Applications. *New J. Chem.*, Vol.30, No.8, pp. 1121-1132, ISSN 1144-0546

Noguez C. (2007). Surface Plasmons on Metal Nanoparticles: the Influence of Shape and Physical Environment. *J. Phys. Chem. C* Vol. 111, No.10, pp. 3806-3819, ISSN 1932-7447

Novoselov, K. S.; Geim, A. K.; Morozov, S. V.; Jiang, D.; Zhang, Y.; Dubonos, S. V.; Grigorieva, I. V.; Firsov, A. A. (2004). Electric Field Effect in Atomically Thin Carbon Films. *Science,* Vol. 306, No. 5696, pp. 666-669, ISSN 1095-9203

Ni Z. H., Wang H. M., Kasim J., Fan H. M., Yu T., Wu Y. H., Feng Y. P., and Shen Z. X., (2007). Graphene Thickness Determination Using Reflection and Contrast Spectroscopy. *Nano Lett.* Vol.7, No.9, pp. 2758-2763, ISSN 1530-6984

Okamoto T; Yamaguchi I. (2003). Optical Absorption Study of the Surface Plasmon Resonance in Gold Nanoparticles Immobilized onto a Gold Substrate by Self-assembly Technique. *J. Phys. Chem. B.*, Vol.107, No.38, pp. 10321-10324, ISSN 1520-6106

Ormonde A. D; Hicks ECM.; Castillo J.; Van Duyne RP. (2004). Nanosphere Lithography: Fabrication of Large-area Ag Nanoparticle Arrays by Convective Self-assembly and Their Characterization by Scanning UV-visible Extinction Spectroscopy. *Langmuir*, Vol.20, No.16, pp.6927-6931, ISSN 0743-7463

Palik E. D. (1991). *Handbook of Optical Constants of Solids*, Academic Press, ISBN 0-12-544422-2, New York

Patel D. V.; McGhee C. N. J. (2007). *Clinical and Experimental Opbtbalmology*, Contemporary in Vivo Confocal Microscopy of the Living Human Cornea Using White Light and Laser Scanning Techniques: a Major Review. Vol.35, No.1, pp. 71-88, ISSN 1442-6404

Pinchuk A.; Hilger A.; Plessen G.; Kreibig U. (2004). Substrate Effect on the Optical Response of Silver Nanoparticles. *Nanotechnology*, Vol.15, No.12, pp. 1890-1896, ISSN 0957-4484

Rembe C.; Dräbenstedt A. (2006). Laser-scanning confocal vibrometer microscope: Theory and experiments. *Review of Scientific Instruments,* Vol. 77, No.8, pp. 083702, ISSN 0034-6748

Ribes A. C.; Damaskinos S.; Dixon A. E; Carver G. E; Peng C.; Fauchet P. M.; Sham T. K.; Coulthard I. (1995). Photoluminescence Imaging of Porous Silicon Using a Confocal Scanning laser Macroscope/Microscope. *Appl. Phys. Lett.*, Vol.66, No.18, pp.2321-2323, ISSN 0003-6951

Saijo Y.; Hozumi N.; Lee C.; Nagao M.; Kobayashi K.; Oakada N.; Tanaka N.; Filho E. S.; Sasaki H.; Tanaka M.; Yambe T. (2006). *Ultrasonics*, Vol. 44, pp. e51-e55, ISSN 0041-624X

Schider G.; Krenn J. R.; Hohenau A.; Ditlbacher H.; Leitner A.; Aussenegg F. R.; Schaich W. L.; Puscasu I.; Monacelli B.; Boreman G. (2003). Plasmon Dispersion Relation of Au and Ag Nanowires. *Phys. Rev. B.*, Vol. 68, No. 15, pp. 155427, ISSN 1098-0121

Singh B. K.; Hillier A. C. (2007). Multicolor Surface Plasmon Resonance Imaging of Ink Jet-Printed Protein Microarrays. *Anal. Chem.*, Vol.79, No.14, pp. 5124-5132, ISSN 0003-2700

Tao A.; Kim F.; Hess C.; Goldberger J.; He R. R.; Sun Y. G.; Xia Y. N.; Yang P. D. (2003). Langmuir-Blodgett Silver Nanowire Monolayers for Molecular Sensing Using Surface-enhanced Raman Spectroscopy. *Nano Letters*, Vol.3, No.9, pp. 1229-1233, ISSN 1530-6984

Veshapidze G.; Trachy M. L.; Shah M. H.; DePaola B. D. (2006). Reducing the Uncertainty in Laser Beam Size Measurement with a Scanning Edge Method. *Appl. Opt.*, Vol.45, No.32, pp. 8197-8199, ISSN 0003-6935

Verveer P. J.; Swoger J.; Pampaloni F.; Greger K.; Marcello M.; Stelzer E. H. K. (2007). High-Resolution Three-Dimensional Imaging of Large Specimens with Light Sheet–Based Microscopy. *Nature Methods,* Vol. 4, No. 4, pp. 311-313, ISSN 1548-7091

Wang Y. Y.; Ni Z. H.; Liu L.; Liu Y. H.; Cong C. X.; Yu T.; Wang X. J.; Shen D. Z.; and Shen Z. X. (2010). Stacking-dependent Optical Conductivity of Bilayer Graphene, *Acs Nano*, Vol.4, No.7, pp. 4074-4080, ISSN 1936-0851

Wang Z. H.; Liu J. W.; Chen X. Y.; Wan J. X.; Qian Y. T. (2004). A Simple Hydrothermal Route to Large-Scale Synthesis of Uniform Silver Nanowires. *Chem. Eur. J.*, Vol.11, No.1, pp. 160-163, ISSN 1521-3765

Wind M. M.; Vlieger J.; Bedeaux D. (1987). The Polarizability of a Truncated Sphere on a Substrate. *Physica A.*, Vol.141, pp. 33-57, ISSN 0378-4371

Youk Y. C.; Kim D. Y. (2006). A Simple Reflection-type Two-dimensional Refractive Index Profile Measurement Technique for Optical Waveguides. *Opt. Comm.*, Vol.262, No.2, pp. 206-210, ISSN 0030-4018

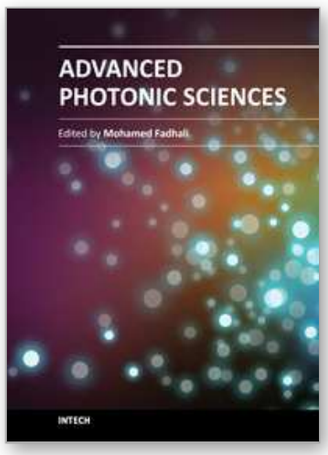

Advanced Photonic Sciences

Edited by Dr. Mohamed Fadhali

ISBN 978-953-51-0153-6
Hard cover, 374 pages
Publisher InTech
Published online 21, March, 2012
Published in print edition March, 2012

The new emerging field of photonics has significantly attracted the interest of many societies, professionals and researchers around the world. The great importance of this field is due to its applicability and possible utilization in almost all scientific and industrial areas. This book presents some advanced research topics in photonics. It consists of 16 chapters organized into three sections: Integrated Photonics, Photonic Materials and Photonic Applications. It can be said that this book is a good contribution for paving the way for further innovations in photonic technology. The chapters have been written and reviewed by well-experienced researchers in their fields. In their contributions they demonstrated the most profound knowledge and expertise for interested individuals in this expanding field. The book will be a good reference for experienced professionals, academics and researchers as well as young researchers only starting their carrier in this field.

InTech Europe
University Campus STeP Ri
Slavka Krautzeka 83/A
51000 Rijeka, Croatia
Phone: +385 (51) 770 447
Fax: +385 (51) 686 166
www.intechopen.com

InTech China
Unit 405, Office Block, Hotel Equatorial Shanghai
No.65, Yan An Road (West), Shanghai, 200040, China
中国上海市延安西路65号上海国际贵都大饭店办公楼405单元
Phone: +86-21-62489820
Fax: +86-21-62489821

IntechOpen